

Article

Research on the Multifactor Synergistic Corrosion of N80 and P110 Steel Tubing in Shale Gas Wells in Sichuan Basin

Yufei Li ¹, Dajiang Zhu ^{1,*} , Jian Yang ¹, Qiang Liu ², Lin Zhang ¹, Linfeng Lu ¹, Xiangkang Liu ¹ and Shuai Wang ¹

¹ Engineering Technology Research Institute, PetroChina Southwest Oil & Gasfield Company, Chengdu 610017, China; L_yf@petrochina.com.cn (Y.L.); gh5525252@gmail.com (J.Y.); zhanglin2018@petrochina.com.cn (L.Z.); lulinfeng@petrochina.com.cn (L.L.); liuxk@petrochina.com.cn (X.L.); wangshuai2022@petrochina.com.cn (S.W.)

² PetroChina Southwest Oil & Gasfield Company, Chengdu 610051, China; xvj333@126.com

* Correspondence: zhu_dj@petrochina.com.cn; Tel.: +86-135-689-86157

Abstract: We aimed to investigate the corrosion patterns and the main controlling factors of N80 steel and P110 steel tubing under different sections. Conducting weight loss corrosion experiments for 168 h using high-temperature and high-pressure autoclaves to simulate the corrosion behavior of two types of casing materials, N80 steel and P110 steel, in different well sections under specific conditions of CO₂ content, chloride ion concentration, temperature, pressure, and sulfate-reducing bacteria population in highly mineralized formation water. X-ray diffraction (XRD), scanning electron microscopy (SEM), and energy-dispersive X-ray spectroscopy (EDS) were used to analyze the corrosion products, surface morphology, and elemental composition of the two steel pipes. Additionally, 3D microscopy was employed to observe the morphology and measure the dimensions of localized corrosion pits. Under different well sections, the corrosion products formed on N80 steel and P110 steel mainly consist of FeCO₃, and crystalline salts of chlorides present in the solution medium. Under low-water-cut conditions, narrow and deep corrosion defects were observed, while narrow and shallow corrosion defects were found under high-water-cut conditions. In the upper wellbore section, both steel pipes exhibited dispersed and thin corrosion product films that suffered from rupture and detachment, resulting in severe localized corrosion. In the middle wellbore section, the corrosion product film on N80 steel comprised irregularly arranged polygonal grains, some of which exhibited significant gaps, leading to extremely severe corrosion. For P110 steel, the corrosion product film was also dispersed and thin, with extensive detachment and extremely severe corrosion. In the lower wellbore section, both steel pipes were covered with a dense layer of grains, with smaller gaps between them, effectively protecting the metal matrix from corrosion. Consequently, the corrosion rate decreased compared to the middle section but still exhibited severe corrosion. In low-water-cut conditions, attention should be given to the risk of column safety due to corrosion from condensate water and CO₂, as well as the size of narrow and deep corrosion defects in the middle wellbore section. In high-water-cut conditions, it is recommended to use corrosion inhibitors in combination while focusing on SRB bacteria corrosion in the upper wellbore section, condensate water in the middle section, CO₂ content and chloride ion coupling in the lower section, and the size of narrow and shallow corrosion defects causing column safety risks.

Keywords: shale gas wells; tubing; CO₂ corrosion; corrosion mechanism; main controlling factors of corrosion



Citation: Li, Y.; Zhu, D.; Yang, J.; Liu, Q.; Zhang, L.; Lu, L.; Liu, X.; Wang, S. Research on the Multifactor Synergistic Corrosion of N80 and P110 Steel Tubing in Shale Gas Wells in Sichuan Basin. *Processes* **2024**, *12*, 920. <https://doi.org/10.3390/pr12050920>

Academic Editor: Albert Ratner

Received: 4 December 2023

Revised: 18 April 2024

Accepted: 23 April 2024

Published: 30 April 2024



Copyright: © 2024 by the authors. Licensee MDPI, Basel, Switzerland. This article is an open access article distributed under the terms and conditions of the Creative Commons Attribution (CC BY) license (<https://creativecommons.org/licenses/by/4.0/>).

1. Introduction

Due to the high content of acidic gases in oil and gas fields in western China, along with high chloride ion concentration and high mineralization [1], such as in the Changning shale gas block in Sichuan, the conditions and technologies for shale gas extraction are more stringent compared to conventional natural gas [2]. Particularly, for downhole tubulars,

their complex and harsh operating conditions can cause intricate and severe corrosion, including pitting corrosion [3], stress corrosion cracking (SCC) [4], microbiologically influenced corrosion (MIC) [5], and multifactor coupled corrosion [6,7]. Low carbon alloy steel is affected by various environmental factors, such as temperature, CO₂ partial pressure, flow rate, and pH value, which can lead to corrosion perforation and reduced strength, posing column safety risks [8,9]. Huang et al. [10] studied the influence of temperature on the corrosion behavior of N80 and TP125V steel in CO₂-saturated shale gas fracturing fluid environments. The results showed that the corrosion rates of N80 and TP125V steel first increased and then decreased with an increasing temperature, reaching the highest value at 100 °C. When the temperature was below 70 °C, the corrosion product film exhibited a porous and loose structure, which was ineffective in preventing solution permeation [11,12]. Yan et al. [13] found that an increase in CO₂ solubility would lead to a higher concentration of dissolved H₂CO₃ in the solution, resulting in an elevation of H⁺ and CO₃²⁻ concentrations from carbonate decomposition, thus accelerating the chemical process of carbon steel's cathodic corrosion and increasing its corrosion rate. On the other hand, the increased CO₂ solubility led to improved densification of the corrosion product film, hindering the penetration of the corrosion medium, thereby reducing the corrosion rate. As the CO₂ partial pressure increased, the protective effect of the CO₂ corrosion product film increased, mainly by altering the FeCO₃ supersaturation [14]. Li et al. [15] conducted a study on the CO₂ corrosion kinetics of N80 steel, revealing an exponential decrease in corrosion rate with increasing corrosion time. Han et al. [16] analyzed the failure of N80 new tubing with early-stage corrosion perforation and found that oxygen corrosion occurred in N80 pipes in CO₂ and O₂ environments, while Cl⁻ intensified pitting development, and the joint action of CO₂, O₂, and Cl⁻ in the operational environment eventually led to pipe corrosion perforation. Yue et al. [17] analyzed the corrosion causes of a shale gas wellbore column, indicating that the shallow section of the wellbore column suffered from bacterial corrosion due to abundant sulfate-reducing bacteria reproduction at lower temperatures, whereas in the deep section, the high environmental temperature effectively suppressed sulfate-reducing bacteria activity, resulting in uniform corrosion mainly caused by CO₂. Liu et al. [18] showed that sulfate-reducing bacteria (SRB) biofilm easily formed on the pipe wall surface and caused localized corrosion under flowing conditions. A mixture of SRB and iron-oxidizing bacteria (IOB) could also synergistically accelerate localized corrosion.

This study investigates the corrosion mechanisms in different sections of tubing, identifying the main controlling factors for corrosion in each section. By providing a theoretical basis for corrosion prevention in N80 and P110 steel tubing in Sichuan shale gas wells, this research contributes to the secure and efficient development of shale gas on a large scale [19–22].

2. Experiment

2.1. Experimental Materials

The experimental materials consist of N80 steel and P110 steel, which are used for oil casings, as shown in Table 1.

Table 1. Composition of common steel used in the experiment (wt%).

P110 Chemical Composition (wt%)												
C	Si	Mn	Cr	P	S	Mo	Ni	Ti	Al	V	Nb	Fe
0.260	0.230	0.520	0.440	0.011	0.020	0.020	0.680	0.01	0.003	0.09	0.005	Bal
N80 Chemical Composition (wt%)												
C	Si	Mn	P	S	Mo	Cr	Ni	Fe				
0.24	0.22	1.50	0.013	0.002	0.009	0.037	0.03	Bal				

2.2. Experimental Setup

Figure 1 illustrates the schematic diagram of the experimental setup used to simulate corrosion in different sections of N80 steel and P110 steel tubing. This setup is a self-developed high-temperature and high-pressure circulating flow corrosion test apparatus, capable of reaching a maximum test pressure of 70 MPa and a maximum test temperature of 250 °C. The vessel has a relatively large volume of 8 L and is forged from C276 alloy. During the experimental pressurization stage, N₂ gas is first introduced to test the airtightness of the high-temperature and high-pressure vessel. Next, N₂ is used to purge the deionized water inside the vessel to remove dissolved oxygen, with a deoxygenation time of 40 min per liter, while also eliminating any remaining air in the vessel. The temperature is then raised to the desired experimental temperature, followed by the introduction of CO₂ gas, until the desired experimental pressure is reached. N₂ gas is used to further pressurize the system to the experimental pressure.

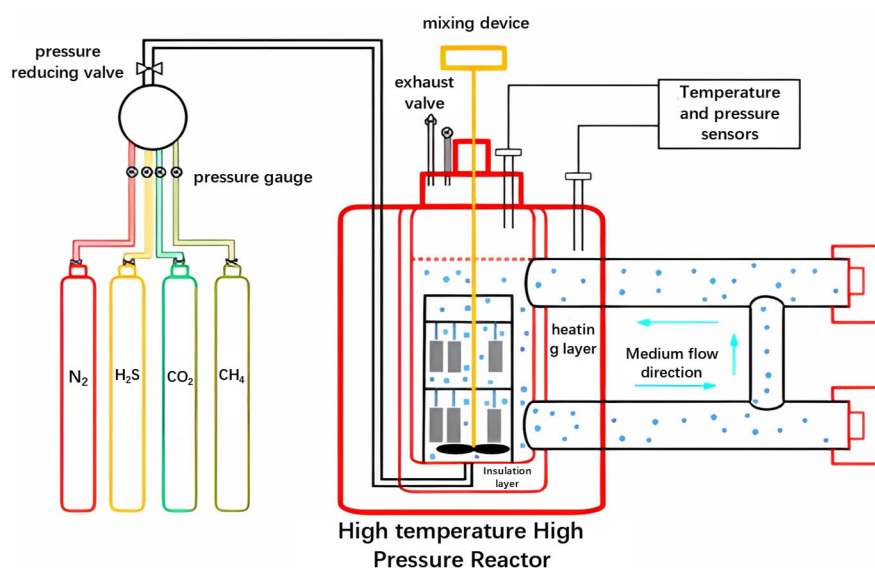


Figure 1. Schematic diagram of high-temperature high-pressure autoclave.

Throughout the experiment, the temperature and pressure of the high-temperature and high-pressure vessel are continuously monitored to ensure that the simulated experimental conditions remain consistent with the actual downhole conditions in oil pipe sections. This sophisticated setup allows for the precise control and replication of the corrosive environment experienced by N80 steel and P110 steel in shale gas wells, providing valuable insights into the corrosion behavior and mechanisms under different wellbore conditions.

2.3. Corrosion Simulation Experiment Method

The samples, consisting of N80 and P110 oil pipe specimens, were processed into corrosion coupons of size 50 mm × 10 mm × 3 mm using a series of steps, including wire cutting, grinding, and polishing. Each experimental group comprised four parallel samples. The samples were cleaned using petroleum ether to remove oil residues, followed by alcohol cleaning to maintain surface cleanliness. Precise measurements of sample weight (with an accuracy of 0.1 mg) and sample dimensions (with an accuracy of 0.01 mm) were performed, and relevant data were recorded. The samples were then securely mounted under the sample holder using polytetrafluoroethylene (PTFE) tape and immersed entirely in the high-temperature and high-pressure vessel.

Each experimental group had four parallel samples, with three samples dedicated to corrosion rate calculations and one sample used for X-ray diffraction (XRD), scanning electron microscopy (SEM), and energy-dispersive X-ray spectroscopy (EDS) analyses.

The corrosion product removal solution is formulated as follows: 10 g of hexamethylenetetramine, 100 mL of hydrochloric acid with a concentration of 12 mol/L, and deionized water added to make a total volume of 1 L. The specific method for removing the corrosion products is as follows: The test samples are placed in a beaker containing the corrosion product removal solution and then placed in an ultrasonic cleaning device for cleaning. After ultrasonic cleaning, the samples are further scrubbed until the surface corrosion products are completely removed. The cleaning procedure follows the standard GB/T 16545-2015 [23].

After the corrosion products are completely removed, the samples are immediately rinsed in tap water to remove residual acid. Then, they are immersed in a saturated sodium bicarbonate solution for approximately 2 to 3 min for neutralization. After rinsing again with tap water and blotting dry with filter paper, the samples are immersed in anhydrous ethanol or acetone for 3 to 5 min for dehydration. Subsequently, the samples are dried with cold air, allowed to stand for a certain period, and then weighed using an electronic balance (with an accuracy of 0.1 mg). The corrosion rate is calculated using the weight loss method, and the corrosion rate formula is as follows:

$$CR = \frac{3.65 \times 10^5 \times (W_1 - W_2)}{ATD} \quad (1)$$

In the formula:

CR: Corrosion rate, expressed in mm/a (millimeters per year).

W_1 : Initial weight of the specimen before the experiment, measured in grams (g).

W_2 : Weight of the specimen after the experiment, measured in grams (g).

A: Surface area of the specimen, measured in mm² (square millimeters).

T: Duration of the experiment, measured in days (d).

D: Material density, measured in g/cm³ (grams per cubic centimeter).

After the corrosion rate calculation is completed, three parallel samples are selected for the observation and 3D microscopic analysis of localized pitting corrosion. The purpose is to examine whether the samples exhibit localized pitting corrosion, observe the surface morphology of the corroded areas, and measure the size of the pitting corrosion features, including the pit mouth width and pit depth data.

3. Corrosion Analysis of N80 Steel and P110 Steel by Weight Loss Method

Weight loss corrosion tests were conducted on N80 steel and P110 steel by simulating their exposure to high salinity formation water in different wellbore conditions using a high-temperature and high-pressure vessel. The vessel was used to immerse the samples for 168 h under specific conditions of CO₂ content, chloride ion concentration, temperature, pressure, and the presence of sulfate-reducing bacteria. The experimental conditions corresponding to different wellbore sections are presented in Table 2, and the average corrosion rates obtained from the tests are shown in Figure 2.

Table 2. Experimental conditions for different wellbore sections.

Tubing Section	Temperature	Pressure	CO ₂	Cl ⁻	SRB
	°C	MPa	%	mg/L	×10 ³ /mL
Upper section	50	10	1.0	10,000	11
Middle section	110	60	1.5	15,000	6
Bottom section	155	90	2.0	20,000	0

In a liquid phase environment, the corrosion rates of N80 steel and P110 steel in the upper wellbore section of the oil pipe are 1.0869 mm/a and 0.6650 mm/a, respectively, both falling within the severe corrosion range. Furthermore, the localized corrosion of N80 steel is more severe than that of P110 steel. In the middle wellbore section, the corrosion rates of both N80 steel and P110 steel reach their maximum values, with rates of 1.7758 mm/a and

1.6272 mm/a, respectively, falling into the extremely severe corrosion range. In the bottom wellbore section, the corrosion rates of N80 steel and P110 steel are 0.6015 mm/a and 0.5945 mm/a, respectively, categorized as severe corrosion. It is observed that in the liquid phase corrosion environment, the corrosion rate of N80 steel is higher than that of P110 steel, and overall, both exhibit severe corrosion rates or above. Therefore, it is recommended to use corrosion inhibitors in high water content well conditions. Additionally, attention should be paid to the corrosion caused by sulfate-reducing bacteria in the upper wellbore section, condensate water in the middle wellbore section, and the coupling effects of CO₂ content and chloride ions in the lower wellbore section, as these factors may lead to potential safety risks in the oil pipe column.

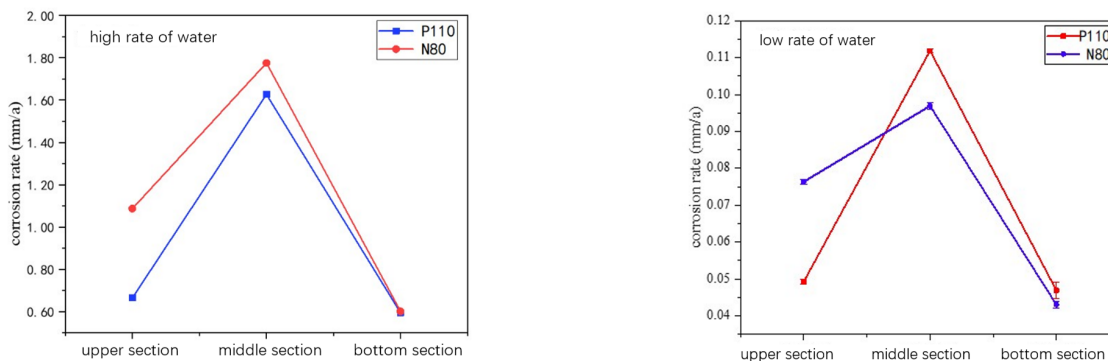


Figure 2. Corrosion changes in different well sections under operating conditions.

In a gas phase environment, the corrosion rates of N80 steel and P110 steel fall into the moderate corrosion range, and there is not much difference in corrosion rates among different wellbore sections. Similarly, in the middle wellbore section of the oil pipe, the uniform corrosion rate reaches its maximum value. The corrosion rates of N80 steel and P110 steel are 0.0969 mm/a and 0.1119 mm/a, respectively. Therefore, in low water content well conditions, it is important to pay attention to the safety risks in the oil pipe column caused by condensate water and CO₂ corrosion in the middle wellbore section.

4. Corrosion Morphology and Phase Analysis of Corrosion Products

N80 steel, under different environmental conditions in the oil pipe wellbore, exhibited varying surface corrosion morphologies after undergoing 168 h of corrosion in the high-temperature and high-pressure vessel. The microstructures of the corrosion products at different magnifications are shown in the figure, indicating significant differences in the morphologies after corrosion under different environmental conditions, as shown in Figure 3.

Under the upper wellbore condition in the oil pipe (temperature: 50 °C, pressure: 10 MPa), the sample surface experienced localized corrosion. The formed corrosion product film exhibited dispersion and had a relatively thin thickness, with ruptures and peeling phenomenon observed. In the middle wellbore condition of the oil pipe (temperature: 110 °C, pressure: 60 MPa), the sample surface showed polygonal grains with a disorderly arrangement, and some areas had larger gaps between grains. Chloride ions (Cl⁻) had a strong penetrating ability and tended to accumulate at interfaces, easily entering the corrosion product film through such gaps and further corroding the N80 steel matrix, exacerbating the corrosion. Under the bottom wellbore condition of the oil pipe (temperature: 155 °C, pressure: 90 MPa), SEM analysis revealed that the sample surface was covered by a dense layer of grains, with very small gaps between the grains. This provided strong isolation and protection to the metal substrate. The dissolution of FeCO₃ corrosion product film displayed a negative temperature effect, meaning that its solubility decreased with an increasing environmental temperature. As a result, Fe²⁺ and CO₃²⁻ in the corrosion medium tended to reach saturation and continuously precipitate. Additionally, chloride

salt crystals adhered to the corrosion product film, increasing its thickness and density. Therefore, the corrosion rate decreased under this condition.

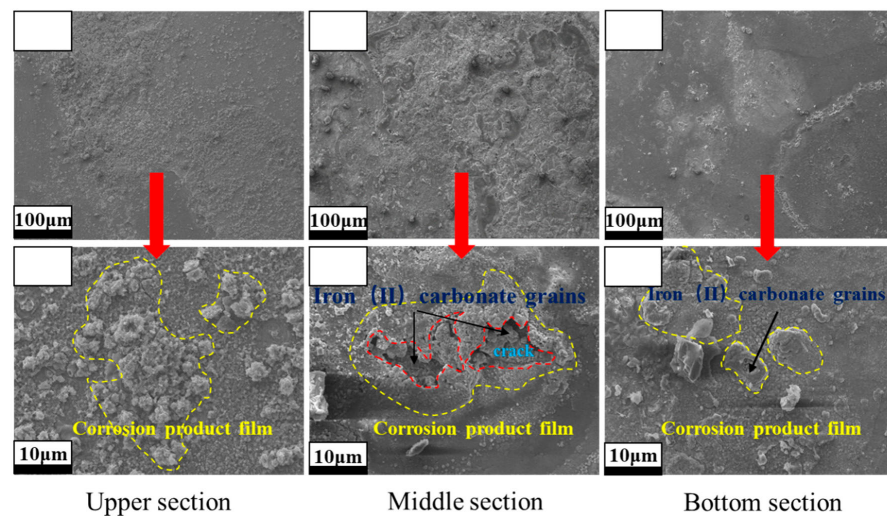


Figure 3. The SEM morphology of the surface corrosion product on N80 steel.

Under different environmental conditions in the oil pipe wellbore, P110 steel exhibits varying corrosion behaviors, as shown in Figure 4. Under the upper wellbore condition (temperature: 50 °C, pressure: 10 MPa), localized corrosion occurs on the sample surface, and the localized corrosion product film shows cracks. The small radius of chloride ions allows them to easily penetrate the corrosion product film, exacerbating the corrosion of the metal substrate, resulting in a higher corrosion rate. In the middle wellbore condition (temperature: 110° C, pressure: 60 MPa), CO₂ corrosion occurs on the metal substrate. Additionally, the increased chloride ion content disrupts the corrosion product film, allowing chloride ions to enter the metal substrate and intensifying the corrosion. The corrosion product film in this condition also exhibits peeling phenomena. Under the bottom wellbore condition (temperature: 155 °C, pressure: 90 MPa), SEM analysis reveals that the sample surface is covered by a dense layer of grains, with very small gaps between the grains. Chloride salt crystals are also observed attached to the corrosion product film, enhancing its isolation and protection of the metal substrate. As a result, the corrosion rate is lower in this condition.

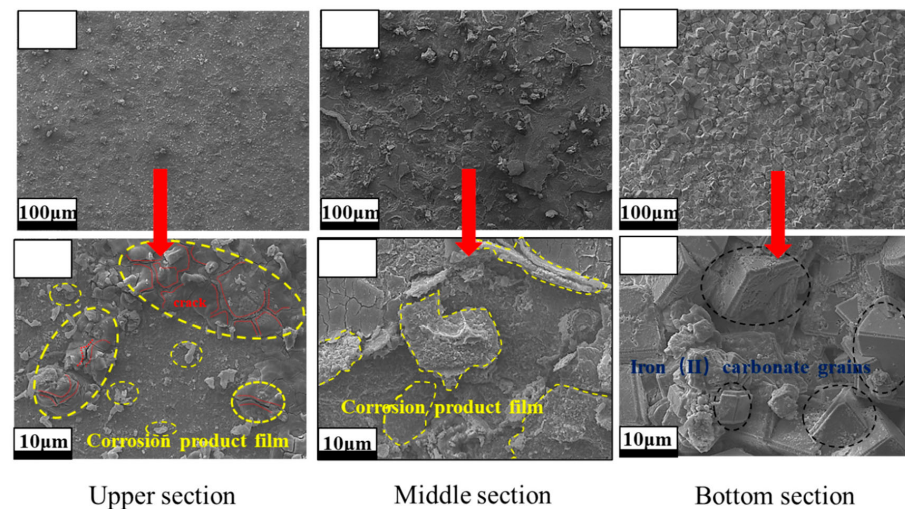


Figure 4. The SEM morphology of the surface corrosion product on P110 steel.

5. EDS Spectrum Analysis of Corrosion Products

The energy spectrum analysis of N80 steel and P110 steel after corrosion under different conditions indicates the presence of three main elements: Fe, C, and O, each with varying mass fractions, as shown in Tables 3 and 4. This observation suggests that under different conditions, N80 steel and P110 steel undergo varying degrees of carbon dioxide corrosion on their localized surfaces, as shown in Figures 5 and 6.

Table 3. Mass fractions of elements in N80 steel (%).

Condition	Element Mass Percentage Fraction %											
	C	O	Na	Si	S	Cl	V	Cr	Mn	Fe	Ni	Cu
50 °C 10 MPa	3.05	21.06	1.81	0.25	—	2.04	—	0.44	0.68	70.57	0.07	0.02
110 °C 60 MPa	8.67	12.6	20.87	—	5.42	18.48	0.17	2.1	0.88	30.02	0.46	0.48
155 °C 90 MPa	7.27	10.6	11.59	0.09	—	4.49	0.21	0.26	1.29	63.98	0.19	0.03

Table 4. Mass percentage of elements in P110 steel (%).

Condition	Element Mass Percentage Fraction %											
	C	O	Na	Si	S	Cl	V	Cr	Mn	Fe	Ni	Cu
50 °C 10 MPa	4.28	28.14	1.1	—	0.35	0.43	0.05	0.88	0.76	63.39	0.38	0.02
110 °C 60 MPa	3.12	27.5	1.8	—	1.52	1.09	0.18	0.91	0.6	63.12	0.01	0.14
155 °C 90 MPa	8.49	28.12	—	0.28	3.41	—	0.09	0.26	0.92	52.81	—	5.07

In the upper wellbore condition, the mass fraction of Fe in N80 steel is 70.57%, C is 3.05%, and O is 21.06%, indicating localized CO₂ corrosion on the N80 steel surface. Additionally, the mass fraction of S is 21.06%, indicating the presence of SRB bacteria, which can survive and reproduce under this condition, leading to SRB bacteria corrosion. The corrosion product film formed under this condition is relatively thin.

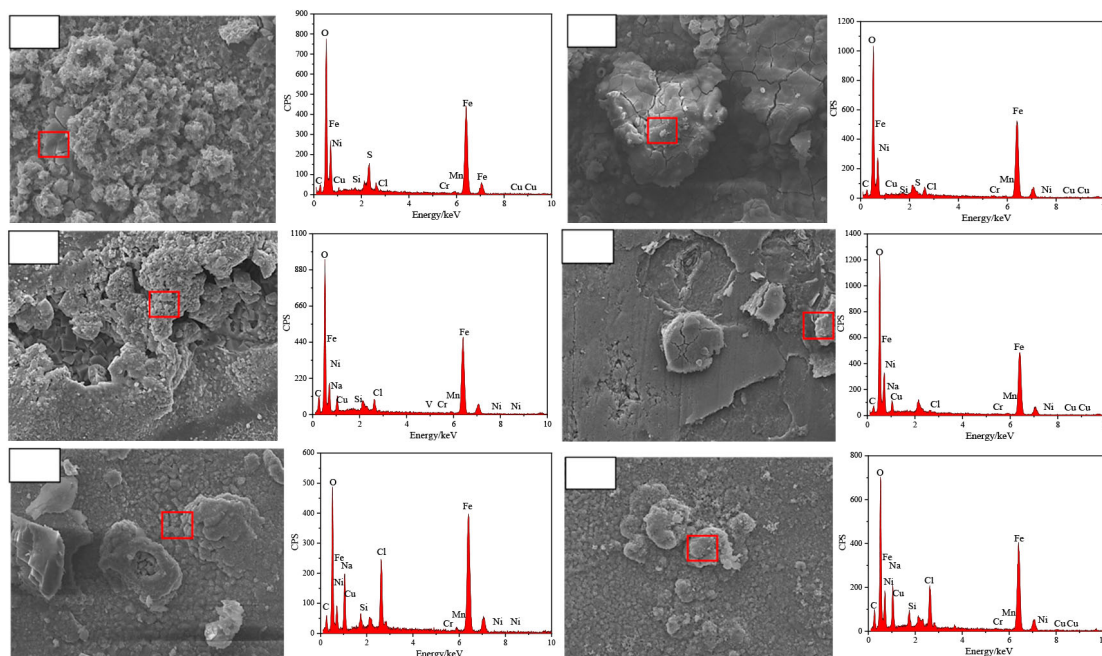


Figure 5. Energy spectrum analysis of EDS products of N80 steel and P110 steel in gas phase medium environment. The scale bar is 10 μ m.

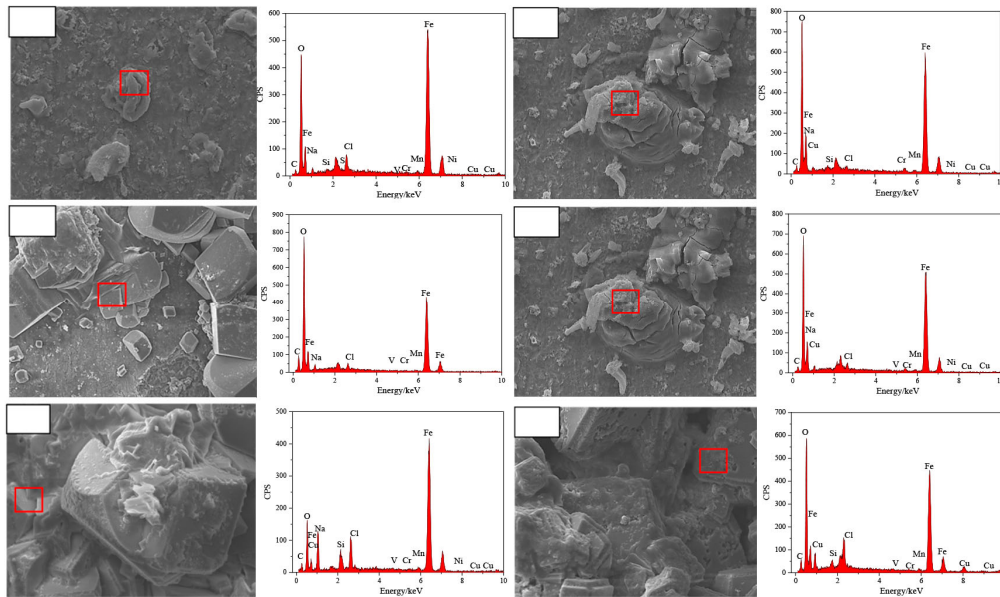


Figure 6. EDS product analysis results of N80 steel and P110 steel in liquid medium environment. The scale bar is 10 μm .

In the middle wellbore condition, the mass fraction of Fe in N80 steel is 30.02%, C is 8.67%, O is 21.06%, Cl is 18.48%, and Na is 20.87%. This indicates that under this condition, CO_2 corrosion on the N80 steel surface is severe, and the corrosion product film contains a significant amount of chloride ions (Cl^-). The presence of many Cl^- ions in the grain boundaries of the corrosion product film leads to its rupture and detachment, further accelerating the corrosion of the metal substrate and increasing the corrosion rate.

In the bottom wellbore condition, the mass fraction of Fe in N80 steel is 63.98%, C is 7.27%, O is 10.6%, and Cl is 4.49%. The lower chloride ion content indicates that the corrosion product film formed on the N80 steel surface is dense and provides effective protection. It effectively prevents chloride ions from entering the metal substrate, leading to a reduction in the corrosion rate.

Through the energy-dispersive X-ray spectroscopy (EDS) analysis of P110 steel after corrosion under different operating conditions (Table 4), it was found that the major elements present were Fe, C, and O, and their mass fractions varied significantly. This indicates that P110 steel experienced varying degrees of carbon dioxide (CO_2) corrosion under different operating conditions.

In the upper section of the wellbore, the mass fractions of Fe, C, and O in N80 steel were found to be 70.57%, 3.05%, and 21.06%, respectively. This indicates that the N80 steel surface experienced localized CO_2 corrosion, and a relatively thin corrosion product film was formed.

In the middle section of the wellbore, the mass fractions of Fe, C, and O in N80 steel were found to be 30.02%, 8.67%, and 21.06%, respectively. Additionally, the mass fractions of Cl and Na were found to be 18.48% and 20.87%, respectively. These results indicate that under this condition, N80 steel surface experienced severe CO_2 corrosion, and the corrosion product film had a relatively high concentration of chloride ions (Cl^-). The presence of a large amount of Cl^- ions in the intergranular spaces of the corrosion product film led to the cracking and detachment of the film, further accelerating the corrosion of the metal substrate, resulting in an increased corrosion rate.

In the bottom section of the wellbore, the mass fractions of Fe, C, and O in N80 steel were found to be 63.98%, 7.27%, and 10.6%, respectively, while the mass fraction of Cl was 4.49%, indicating a lower concentration of chloride ions. This suggests that under this condition, a dense corrosion product film formed on the surface of N80 steel, which

effectively protected the metal substrate by preventing the ingress of chloride ions. As a result, the corrosion rate was reduced.

6. XRD Image Analysis of the Composition of Corrosion Products

At a temperature of 50 °C and pressure of 10 MPa, the XRD spectrum of N80 steel shows a broad and high peak of Fe. This indicates that the corrosion product film is relatively thin, and X-rays can penetrate the corrosion product film to reveal the diffraction pattern of the base metal, as shown in Figure 7. At a temperature of 110 °C and pressure of 60 MPa, the XRD spectrum shows peaks corresponding to Fe, FeCO₃, and chloride salt crystals. This suggests that under this condition, the surface of N80 steel experiences CO₂ corrosion along with the formation of FeCO₃ and chloride salt crystals. Similarly, at a temperature of 155 °C and pressure of 90 MPa, the XRD spectrum also exhibits peaks of Fe, FeCO₃, and chloride salt crystals, indicating that the predominant corrosion mechanism is CO₂ corrosion.

At a temperature of 50 °C and pressure of 10 MPa, the XRD spectrum of P110 steel shows peaks of Fe and a small amount of salt crystals, but no significant corrosion products were detected. At a temperature of 110 °C and pressure of 60 MPa, the XRD spectrum exhibits peaks corresponding to Fe, FeCO₃, and chloride salt crystals, indicating the presence of corrosion products on the surface of the P110 steel under this condition. Similarly, at a temperature of 155 °C and pressure of 90 MPa, the XRD spectrum also shows peaks of Fe, FeCO₃, and chloride salt crystals, indicating that the main corrosion mechanism for the P110 steel is CO₂ corrosion, as shown in Figure 8.

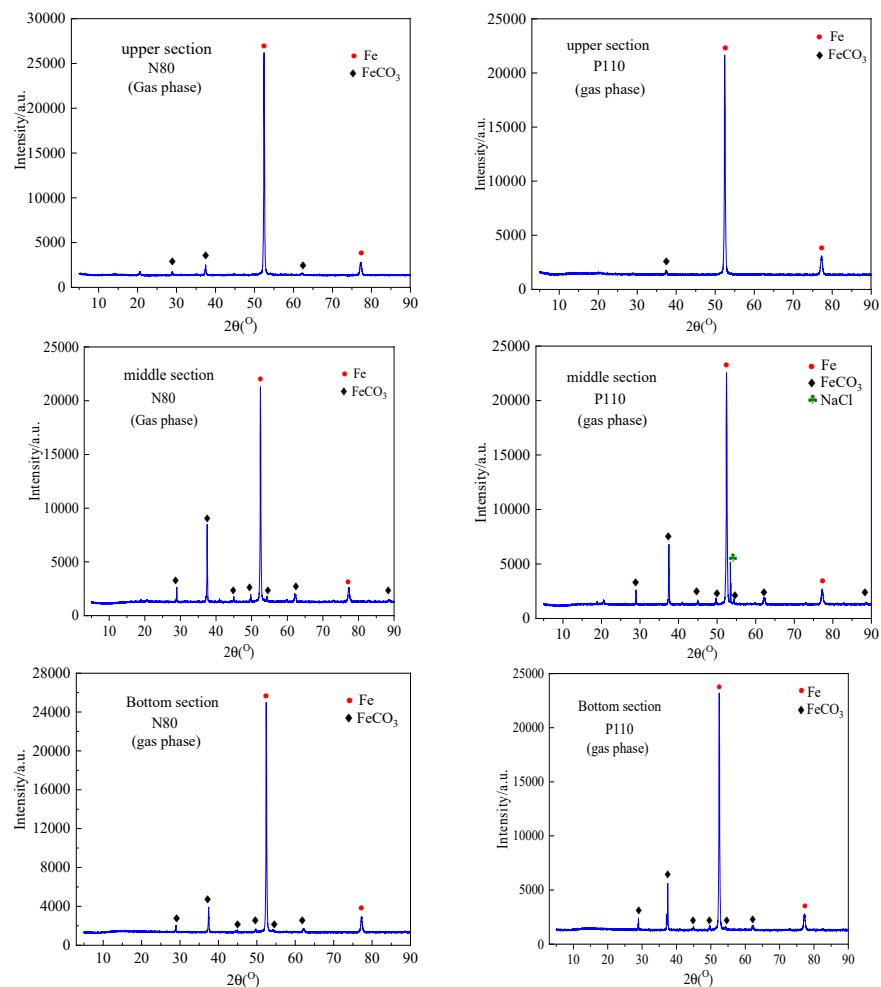


Figure 7. Analysis of XRD corrosion products of N80 steel and P110 steel in gaseous medium environment.

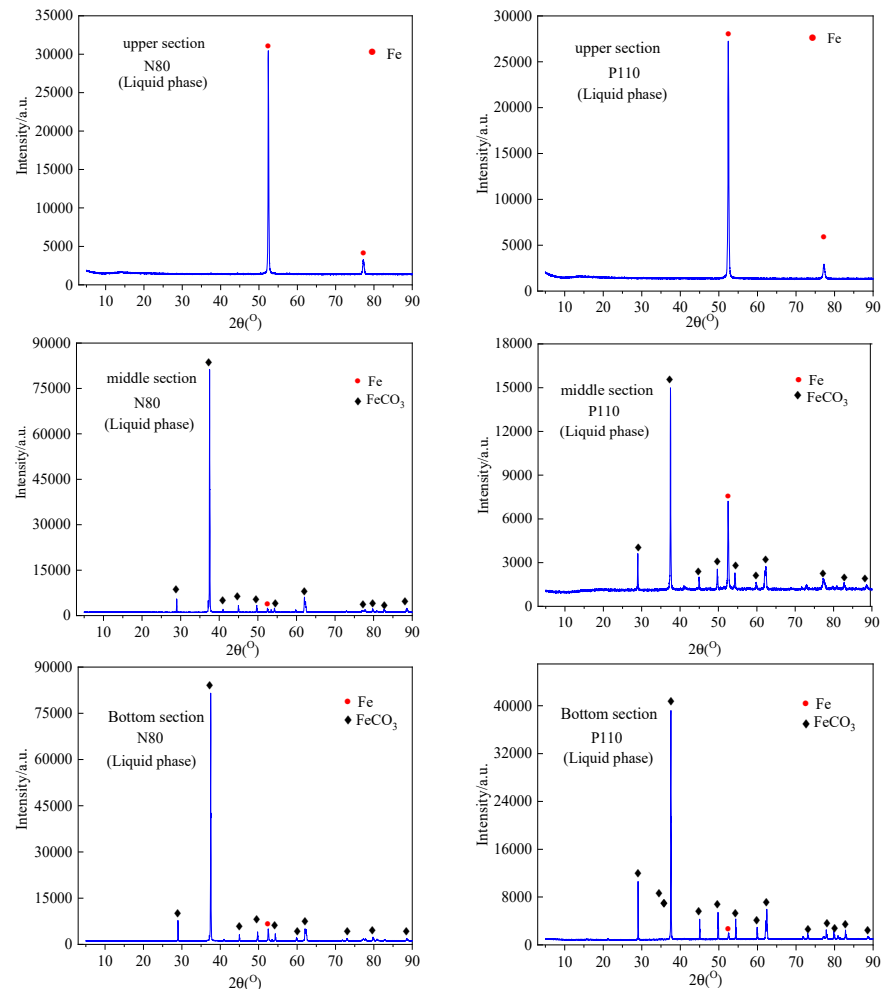


Figure 8. Analysis of XRD corrosion products of N80 steel and P110 steel in liquid medium environment.

7. Change Pattern of Local Corrosion Defects

(1) High water-cut well conditions

At a temperature of 50 °C and pressure of 10 MPa, the surface of P110 steel exhibits relative flatness, with the maximum depth of localized corrosion pits being 2.7 μm and the opening width measuring 0.03 mm. The corrosion on the metal surface under this condition is slight. At a temperature of 110 °C and pressure of 60 MPa, the surface of P110 steel shows overall thinning, with the presence of larger-sized, wide and shallow corrosion pits. The maximum depth of localized corrosion pits is measured at 28.3 μm, and the opening width is 0.26 mm. From the SEM images, it is evident that the corrosion product film on the metal surface is porous and loose, indicating that chloride ions penetrate the pores and accelerate the corrosion of the metal substrate. At a temperature of 155 °C and pressure of 90 MPa, the surface of P110 steel forms a dense corrosion product film, and there are larger-sized, wide, and shallow corrosion pits locally. The maximum depth of localized corrosion pits is 45.0 μm, and the opening width is 0.18 mm.

At a temperature of 50 °C and pressure of 10 MPa, the surface of N80 steel exhibits locally porous and loosely packed corrosion product film, with the maximum depth of localized corrosion pits measuring 4.3 μm and the opening width being 0.17 mm. The corrosion on the metal surface under this condition is relatively severe. At a temperature of 110 °C and pressure of 60 MPa, the surface of N80 steel shows overall thinning, with the presence of larger-sized, wide, and shallow corrosion pits locally. The maximum depth of localized corrosion pits is measured at 2.6 μm, and the opening width is 0.11 mm. From the

SEM images, it is evident that the corrosion product film on the metal surface is porous and loose, indicating that corrosion ions penetrate the pores and accelerate the corrosion of the metal substrate. At a temperature of 155 °C and pressure of 90 MPa, the surface of N80 steel forms a dense corrosion product film, and there are larger-sized, wide, and shallow corrosion pits locally. The maximum depth of localized corrosion pits is 5.6 μm, and the opening width is 0.26 mm.

(2) Low water-cut well conditions

At a temperature of 50 °C and pressure of 10 MPa, the surface of P110 steel appears relatively flat with minimal corrosion, exhibiting narrow and deep corrosion pits locally. The maximum depth of the localized corrosion pits is measured at 2.6 μm, and the opening width is 0.17 mm. At a temperature of 110 °C and pressure of 60 MPa, the surface of P110 steel experiences severe localized corrosion, with some micro-cracks in the corrosion product film. Numerous wide and deep corrosion pits are observed locally, with the maximum depth of the localized corrosion pits measuring 4.7 μm, and the opening width being 0.19 mm. This indicates that corrosion ions penetrate the cracks, accelerating the corrosion of the metal substrate. At a temperature of 155 °C and pressure of 90 MPa, the surface of P110 steel exhibits narrow and deep corrosion pits locally. The maximum depth of the localized corrosion pits is measured at 8.2 μm, and the opening width is 0.08 mm.

At a temperature of 50 °C and pressure of 10 MPa, the surface of N80 steel appears relatively flat with minor corrosion, exhibiting narrow and deep corrosion pits locally. The maximum depth of the localized corrosion pits is measured at 7.9 μm, and the opening width is 0.26 mm. At a temperature of 110 °C and pressure of 60 MPa, the surface of N80 steel experiences severe localized corrosion, with some micro-cracks in the corrosion product film. Numerous wide and deep corrosion pits are observed locally, with the maximum depth of the localized corrosion pits measuring 4.2 μm, and the opening width being 0.25 mm. This indicates that corrosion ions penetrate the cracks, accelerating the corrosion of the metal substrate. At a temperature of 155 °C and pressure of 90 MPa, the surface of N80 steel exhibits localized wide and deep corrosion pits. The maximum depth of the localized corrosion pits is measured at 8.1 μm, and the opening width is 0.12 mm.

In the corrosive environment, the depth of corrosion pits in both N80 steel and P110 steel increases with the rise in temperature and pressure, indicating more severe localized corrosion. In high water cut well conditions, the corrosion pits mainly exhibit a narrow and shallow morphology, while in low water cut well conditions, they mostly appear as narrow and deep pits. Under low water cut well conditions, both N80 steel and P110 steel are prone to develop narrow and shallow corrosion pits. When subjected to high stress loads, they are more likely to experience stress concentration, leading to the corrosion puncture of the oil pipe.

8. Research on CO₂ Corrosion Mechanism

8.1. CO₂ Corrosion Mechanism in Liquid Phase Environment

The mechanism of CO₂ corrosion is generally believed to involve the dissolution of CO₂ in water, forming carbonic acid, which reacts with Fe in the solution, leading to the corrosion of Fe. There are mainly two cathodic corrosion reactions. The anodic corrosion reaction involves the oxidation of Fe to form Fe²⁺ ions, The essence of cathodic reactions is the reduction process where CO₂ dissolves to form HCO₃⁻ ions and releases H⁺ ions. The corrosion mechanism is illustrated in the accompanying diagram.

8.2. CO₂ Corrosion Mechanism in Gas Phase Environment

As the temperature increases, the water in the liquid phase environment evaporates and exists in the gas phase as water vapor. Some water molecules move to the metal surface and condense into water droplets, as shown in Figures 9–11. With CO₂ dissolving in the water droplets, carbonic acid (H₂CO₃) forms, and the reaction between H₂CO₃ and Fe leads to CO₂ corrosion on the metal substrate, as illustrated in Figures 10 and 11. When the content of Fe²⁺ and CO₃²⁻ reaches saturation, continuous precipitation occurs. As the

temperature rises to a certain extent, a corrosion product film composed of FeCO_3 crystals forms, as depicted in Figure 12. At low temperatures, the crystal growth rate on the metal substrate is greater than the nucleation rate, resulting in larger gaps between crystals. These gaps facilitate the aggregation of corrosive ions into the corrosion product film, leading to further corrosion of the metal substrate. In contrast, at high temperatures, the crystal growth rate is lower than the nucleation rate, resulting in the formation of numerous small crystals. Additionally, salt crystals adhere to the corrosion product film, increasing its thickness and compactness, effectively protecting the metal substrate.

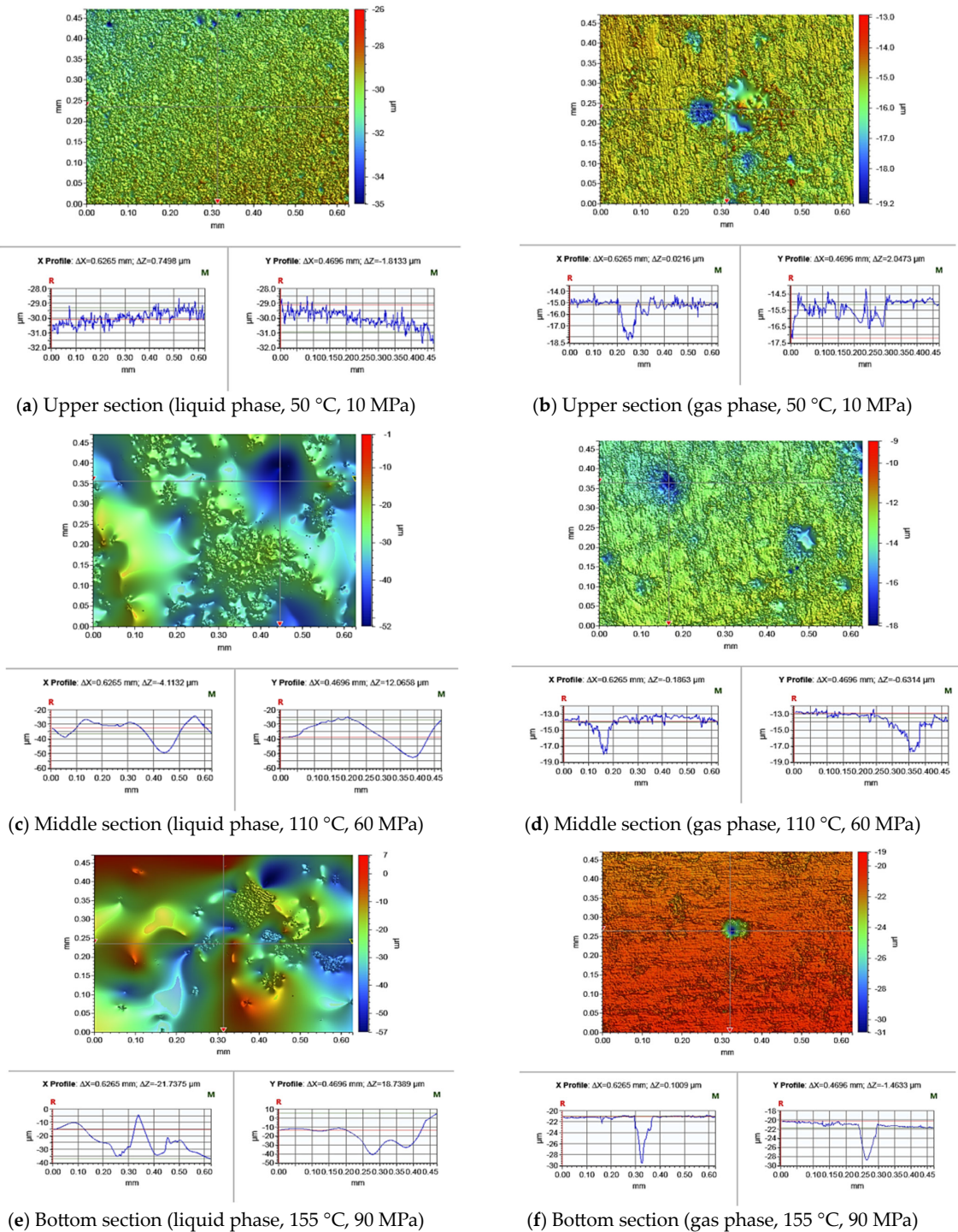


Figure 9. Size and morphology of local corrosion pits on P110 steel.

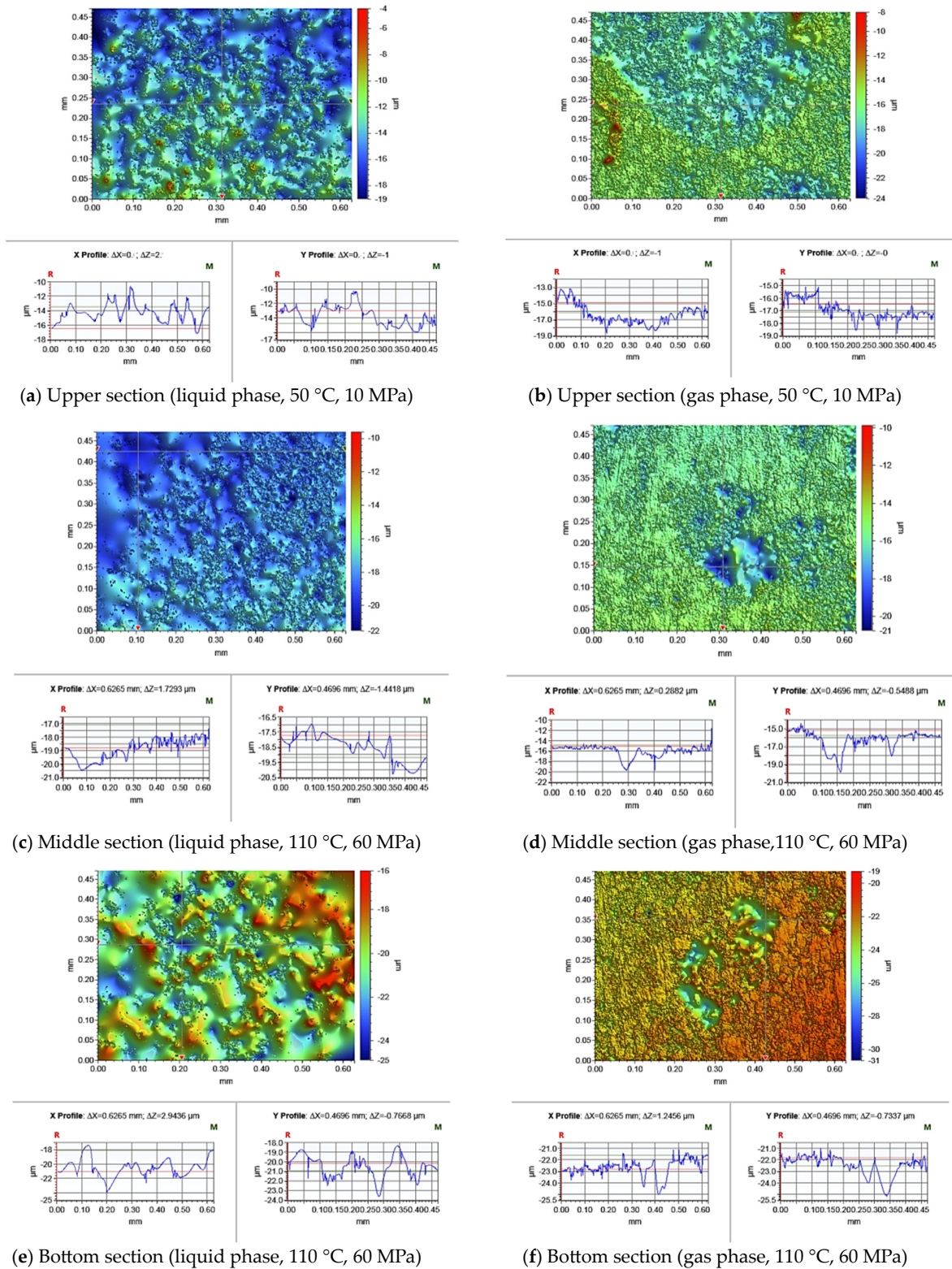


Figure 10. Size and morphology of local corrosion pits on N80 steel.

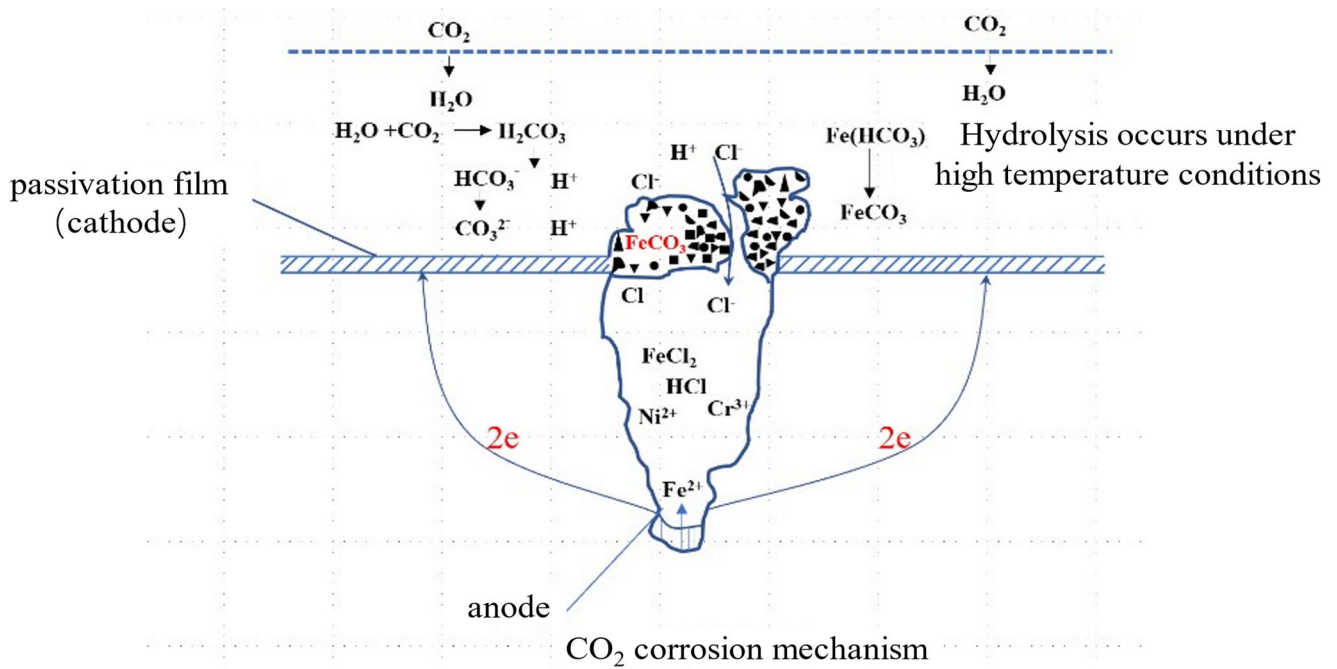


Figure 11. Schematic diagram of CO₂ corrosion mechanism.

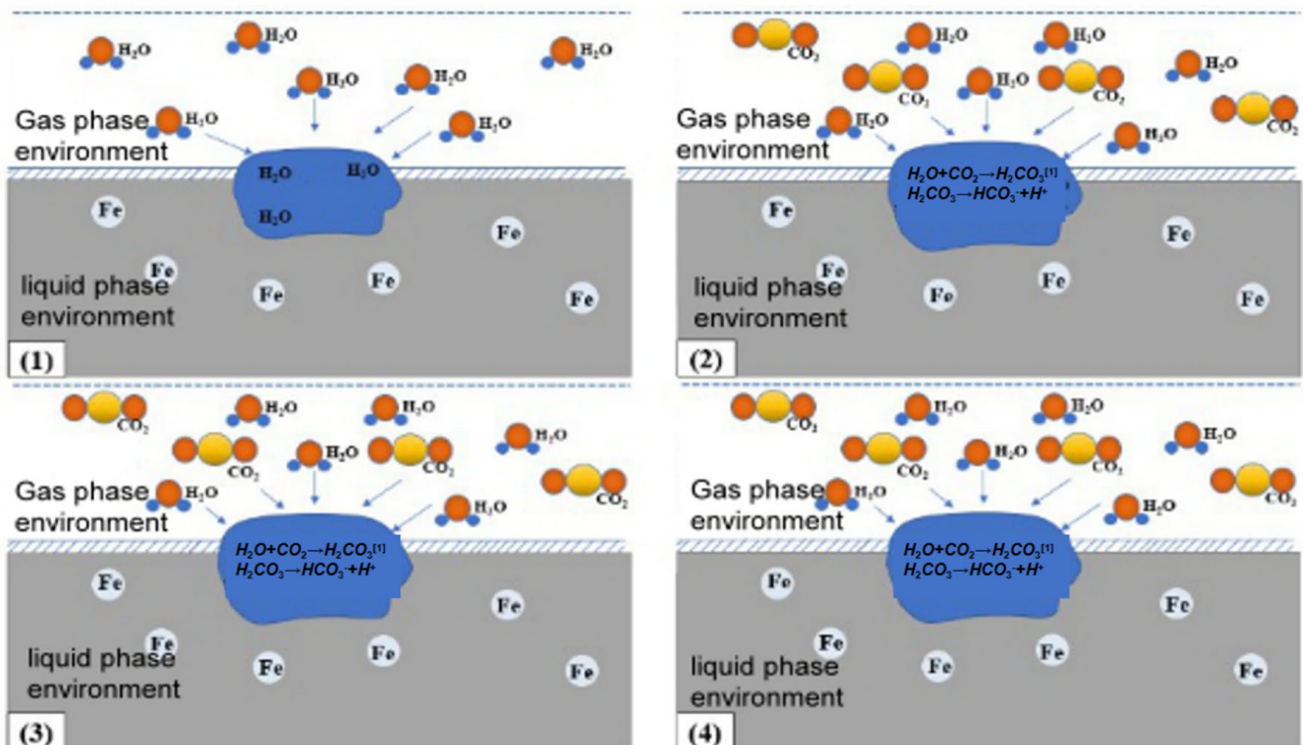


Figure 12. CO₂ corrosion occurs on the surface of the metal substrate. 1: The surface condenses into water droplets. 2: CO₂ dissolves in water droplets to form carbonic acid. 3: CO₂ corrosion. 4: Corrosion product film formation.

9. Conclusions and Recommendations

In shale gas wells, both N80 and P110 steel pipes exhibit the highest uniform corrosion rate in the middle wellbore section and the highest risk of localized corrosion in the lower wellbore section. The main corrosion mechanisms for N80 and P110 steel pipes in shale gas wells are CO₂ and SRB (sulfate-reducing bacteria) corrosion. Under low water content

conditions, the uniform corrosion rate is relatively low, but the formed localized corrosion defects are of narrow and deep types. Therefore, attention should be given to CO₂ corrosion and condensate water-related issues in the middle wellbore section, as well as the risk of failure due to narrow and deep corrosion defects. Under high water content conditions, the uniform corrosion rate is relatively high, and the formed localized corrosion defects are mainly wide and shallow. It is recommended to use corrosion inhibitors in combination to mitigate the corrosion. Moreover, attention should be paid to SRB in the upper section, condensate water in the middle section, CO₂ and chloride ion coupling effects in the lower section, and the risk of column failure induced by defects.

Author Contributions: Methodology, Y.L.; Validation, L.Z., L.L. and X.L.; Formal analysis, D.Z. and S.W.; Investigation, Q.L.; Data curation, J.Y. All authors have read and agreed to the published version of the manuscript.

Funding: This work was funded by the Research of rapid evaluation technology of settling stability of completion fluid for high temperature oil testing in Penglai gas area (20230302-06), the Research and field test on new technology of drainage gas production (2022KT1902).

Data Availability Statement: Data are contained within the article.

Conflicts of Interest: The authors were employed by the PetroChina Southwest Oil & Gasfield Company. The authors declare that there are no conflicts of interest.

References

1. Wang, B.; Xiong, M.; Wang, P. Chemical characterization in hydraulic fracturing flowback and produced water (HF-FPW) of shale gas in Sichuan of China. *Environ. Sci. Pollut. Res.* **2020**, *27*, 26532–26542. [[CrossRef](#)] [[PubMed](#)]
2. Demirbas, A.; Nurettin, C.; Sukru, A. Chemical analyses of shale gas and conventional natural gas. *Petrol. Sci. Technol.* **2018**, *36*, 1690–1695. [[CrossRef](#)]
3. Li, Y.; Xu, N.; Liu, G. Crevice corrosion of N80 carbon steel in CO₂-saturated environment containing acetic acid. *Corros. Sci.* **2016**, *112*, 426–437. [[CrossRef](#)]
4. Li, Y.Z.; Guo, X.P.; Zhang, G.A. Synergistic effect of stress and crevice on the corrosion of N80 carbon steel in the CO₂-saturated NaCl solution containing acetic acid. *Corros. Sci.* **2017**, *123*, 228–242. [[CrossRef](#)]
5. Liu, H.; Gu, T.; Zhang, G.A. Corrosion of X80 pipeline steel under sulfate-reducing bacterium biofilms in simulated CO₂-saturated oilfield produced water with carbon source starvation. *Corros. Sci.* **2018**, *136*, 47–59. [[CrossRef](#)]
6. Wu, T.; Yan, M.; Zeng, D. Stress Corrosion Cracking of X80 Steel in the Presence of Sulfate-reducing Bacteria. *J. Mater. Sci. Technol.* **2015**, *31*, 413–422. [[CrossRef](#)]
7. Chen, X.; Wang, G.; Gao, F. Effects of sulphate-reducing bacteria on crevice corrosion in X70 pipeline steel under disbonded coatings. *Corros. Sci.* **2015**, *101*, 1–11. [[CrossRef](#)]
8. Zhang, Y.; Pang, X.; Qu, S. Discussion of the CO₂ corrosion mechanism between low partial pressure and supercritical condition. *Corros. Sci.* **2012**, *59*, 186–197. [[CrossRef](#)]
9. Eslami, A.; Kania, R.; Worthingham, B. Effect of CO₂ and R-ratio on near-neutral pH stresscorrosion cracking initiation under a disbonded coating of pipeline steel. *Corros. Sci.* **2011**, *53*, 2318–2327. [[CrossRef](#)]
10. Huang, J.H.; Yuan, X.; Chen, W. Effect of Temperature on Corrosion Behavior of Pipeline Steels N80 and TP125V Steel in Artificial CO₂-saturated Fracturing Fluid Environment of Shale Gas. *J. Chin. Soc. Corros. Prot.* **2023**, *43*, 251–260.
11. Schmitt, G. *Advances in CO₂ Corrosion*; CORROSION/85, Paper No. 1; NACE: Houston, TX, USA, 1985.
12. Nyborg, R.; Dugstad, A. *Mesa Corrosion Attack in Carbon Steel and 0.5%Chromium Steel*; CORROSION/98, Paper No. 29; NACE: Houston, TX, USA, 1998.
13. Yan, X.; Lin, Y.H.; Shi, Y.S. Test of CO₂ Solubility and Its Effect on the Corrosion of N80 Steel. *Mater. Prot.* **2022**, *55*, 34–40.
14. Dugstad, A. *The Importance of FeCO₃ Supersaturation on the CO₂ Corrosion of Carbon Steels*; CORROSION/92, Paper No. 92; NACE: Houston, TX, USA, 1992.
15. Li, B.; Ren, C.Q.; Liu, L. Research on the Kinetics of CO₂ Corrosion on N80 Steel. *Mater. Rep.* **2013**, *27*, 116–119.
16. Han, Y.; Ju, Y.F.; Luo, Y.G. Analysis on Corrosion Perforation Failure on New N80 Tubing. *Mater. Prot.* **2020**, *53*, 160–165.
17. Yue, M.; Long, Y.; Zhang, T. Corrosion Causes Analysis of Tubing String Used in a Shale Gas Well. *Pet. Tubul. Goods Instrum.* **2021**, *7*, 84–89.
18. Liu, T.; Cheng, Y.F.; Sharma, M. Effect of fluid flow on biofilm formation and microbiologically influenced corrosion of pipelines in oilfield produced water. *J. Pet. Sci. Eng.* **2017**, *156*, 451–459. [[CrossRef](#)]
19. Li, C.; Wang, C.Q.; Chen, X. Corrosion Law and Protective Measures of Shale Gas Well Wellbores. *Corros. Prot.* **2020**, *41*, 35–40.
20. Liu, G.C.; Sun, Y.T.; Ma, Z.H. Corrosion Behavior of N80 Steel in High-Temperature CO₂ Flowing Fluid Containing. *Mater. Prot.* **2014**, *47*, 68–70.

21. Liu, M. Effect of uniform corrosion on mechanical behavior of E690 high-strength steel lattice corrugated panel in marine environment: A finite element analysis. *Mater. Res. Express* **2021**, *8*, 066510. [[CrossRef](#)]
22. Rehioui, M. Controlling Corrosion Using Non-Toxic Corrosion Inhibitors Anti-Corrosion. *Methods Mater.* **2022**, *28*, 351–361.
23. GB/T 16545-2015; Removal of Corrosion Products from Corroded Metal and Alloy Specimens. General Administration of Quality Supervision and The Standardization Administration of China, Inspection and Quarantine of the People's Republic of China: Beijing, China, 2015.

Disclaimer/Publisher's Note: The statements, opinions and data contained in all publications are solely those of the individual author(s) and contributor(s) and not of MDPI and/or the editor(s). MDPI and/or the editor(s) disclaim responsibility for any injury to people or property resulting from any ideas, methods, instructions or products referred to in the content.